Monthly Notices
of the
ROYAL ASTRONOMICAL SOCIETY

MNRAS **467,** 2517–2528 (2017) doi:10.1093/mnras/stx177

On the mass of the Galactic star cluster NGC 4337

Anton F. Seleznev,[1]★ Giovanni Carraro,[2] Roberto Capuzzo-Dolcetta,[3] Lorenzo Monaco[4] and Gustavo Baume[5,6]

[1]*Astronomical Observatory, Ural Federal University, Mira str. 19, Ekaterinburg 620002, Russia*
[2]*Dipartimento di Fisica e Astronomia, Universitá di Padova, Vicolo Osservatorio 3, I-35122 Padova, Italy*
[3]*Dipartimento di Fisica, Sapienza, Universitá di Roma, P.le A. Moro 5, I-00165 Roma, Italy*
[4]*Departamento de Ciencias Fisícas, Universidad Andres Bello, Republica 220, Santiago, Chile*
[5]*Facultad de Ciencias Astronómicas y Geofísicas (UNLP), Universidad de La Plata (CONICET, UNLP), Paseo del Bosque s/n, La Plata, Argentina*
[6]*Instituto de Astrofísica de La Plata (CONICET, UNLP), Paseo del Bosque s/n, La Plata, Argentina*

Accepted 2017 January 19. Received 2017 January 18; in original form 2016 April 28

ABSTRACT

Only a small number of Galactic open clusters survive for longer than a few hundred million years. Longer lifetimes are routinely explained in term of larger initial masses, particularly quiet orbits and off-plane birthplaces. We derive in this work the actual mass of NGC 4337, one of the few open clusters in the Milky Way inner disc that has managed to survive for about 1.5 Gyr. We derive its mass in two different ways. First, we exploit an unpublished photometric data set in the *UBVI* passbands to estimate – using star counts – the cluster luminosity profile, luminosity and mass function and hence its actual mass from both the luminosity profile and mass function. This data set is also used to infer crucial cluster parameters, such as the cluster half-mass radius and distance. Secondly, we make use of a large survey of cluster star radial velocities to derive dynamical estimates for the cluster mass. Using the assumption of virial equilibrium and neglecting the external gravitational field leads to values for the mass significantly larger than those obtained by means of the observed density distribution or with the mass function, but still marginally compatible with the inferred values of invisible mass in the form of both low-mass stars and remnants of high-mass stars in the cluster. Finally, we derive the cluster initial mass by computing the mass loss experienced by the cluster during its lifetime and adopting the various estimates of the actual mass.

Key words: open clusters and associations: general – open clusters and associations: individual: NGC 4337.

1 INTRODUCTION

NGC 4337 is an intermediate-age, metal-rich, open cluster that recently received some attention, being a rare example of an old, metal-rich star cluster located in the inner regions of the Galactic disc.

The first CCD study by Carraro et al. (2014a) pointed out the potential interest of this object. Then a spectroscopic follow-up of the cluster red giant clump stars with the Ultraviolet and Visual Echelle Spectrograph at the Very Large Telescope (UVES@VLT) by Carraro, Monaco & Villanova (2014b) indicated that NGC 4337 is richer in metals than the Sun and 1.6 Gyr old. In that work, a comparison was performed with a typical example of an intermediate-age, metal-rich open cluster, NGC 752. The comparison is particularly intriguing. Actually, NGC 752 and NGC 4337 share the same age and metal composition, although they have very different physical structure. NGC 752 (Twarog et al. 2015) is a star cluster on the brink of dissolution, as one can judge from its main sequence (MS), which is heavily depleted in stars a few magnitudes below the turn-off (TO) point. The cluster also appears on maps as a diffuse agglomeration of stars, hardly distinguishable from the general Galactic field. NGC 752 owes its discovery and fortune to its particular present-day location, high over the Galactic plane. On the other hand, NGC 4337 is located close to the Galactic plane but appears as a strong star concentration when compared with the surrounding field. Its MS does not show any evidence of low-mass star depletion to the limit of actual photometry. One may wonder whether the different dynamical evolution of the two clusters is due to several facts. First of all, they may have formed with very different initial masses and for this reason, after the very same time, NGC 752 is much more dynamically *evolved* than NGC 4337. Secondly and assuming that they were born with the same initial mass, it might be that the orbits of these two clusters were very different and NGC 752 experienced the effects of Galaxy tidal forces more strongly. Finally, the two clusters could have had the same mass at birth and

★ E-mail: anton.seleznev@urfu.ru

undergone a similar degree of interaction with the Galaxy but might have originally had a significantly different structure.

In an attempt to cast more light on this topic, in this work we exploit an unpublished photometric data set in *UBVI* and multi-object spectroscopic observations obtained with GIRAFFE@VLT to derive an estimate of the present-day mass of NGC 4337. We first estimate the luminous mass using the star density profile and star luminosity function. Then we estimate the dynamical mass using the velocity dispersion of stars, both with the assumption of virial equilibrium and taking into account possible non-stationarity of the cluster and Galactic gravitational field. Note that virial equilibrium is a commonly accepted condition for star clusters (Davies et al. 2011; Tofflemire et al. 2014; Geller, Latham & Mathieu 2015). In anticipation of the results, we found that the dynamical (virial) mass is a factor of 5 larger than the luminous mass and we discuss the different possible explanations.

The article is organized as follows. In Section 2, we describe how we collect and reduce the photometric data used in this work. Section 3 deals with the spectroscopic observations and reduction. The distance to NGC 4337 is discussed in Section 4. Then Section 5 is dedicated to estimating the cluster centre and its radius. This, together with the distance, are crucial to estimate the luminous and dynamical mass of the cluster. Sections 6, 7 and 8 illustrate how we derive the luminous mass from the cluster radial density profile and luminosity and mass function. The derivation of the dynamical mass is discussed in Section 9. Finally, Section 10 summarizes our results and provides some discussion.

2 PHOTOMETRIC OBSERVATIONS

We took multiple *UBVI* images of NGC 4337 in a 20 × 20 arcmin^2 area on 2006 March 21 at Cerro Tololo Inter-American Observatory (CTIO), using the 1.0-m ex-Yalo telescope, operated by the SMARTS consortium.[1] This camera is equipped with an STA 4064 × 4064 CCD[2] with 15-μm pixels, yielding a scale of 0.289 arcsec pixel^{-1} and a field of view (FOV) of 20 × 20 arcmin^2 at the Cassegrain focus of the telescope. This FOV is large enough to cover the whole cluster and to sample the surrounding Galactic field. This is visible in Fig. 1, where we show CCD image for the NGC 4337 field.

In Table 1 we present the log of our observations. All observations were carried out in photometric, good-seeing conditions. Our *UBVI* instrumental photometric system was defined by the use of a standard broad-band Kitt Peak $UBVI_{kc}$ set of filters.[3] To determine the transformation from our instrumental system to the standard Johnson–Kron–Cousins system and to correct for extinction, each night we observed Landolt's area PG 1047 and SA 101, SA 104, and SA 107 (Landolt 1992) multiple times and with different airmasses.

Basic calibration of the CCD frames was done using the Yale/SMARTS Y4K reduction script based on the IRAF[4] package CCDRED and the photometry was performed using IRAF's DAOPHOT and PHOTCAL packages. Instrumental magnitudes were extracted using the point-spread function (PSF) method (Stetson 1987) and adopting a quadratic, spatially variable master PSF. Finally, the

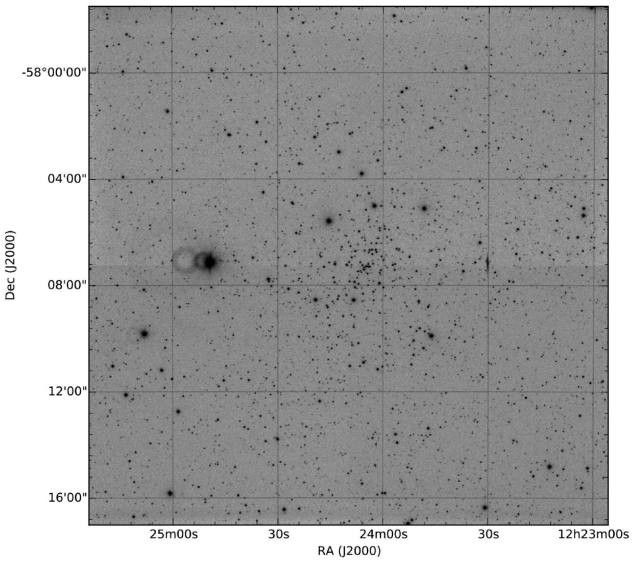

Figure 1. A 120-s frame in *B* for NGC 4337. North is up, east to the left. The field is 20 arcmin on a side.

Table 1. *UBVI* photometric observations of NGC 4337 and Landolt standard stars on 2006 March 21.

Field	Filter	Exposures (s)	Airmass (*X*)
NGC 4337	*U*	10, 30, 200, 1800	1.19–1.25
	B	7, 30, 100, 900	1.15–1.25
	V	5, 30, 100, 700	1.16–1.25
	I	5, 30, 100, 600	1.17–1.25
SA 101	*U*	2 × 400	1.20–1.24
	B	2 × 200	1.19–1.22
	V	2 × 150	1.19–1.22
	I	2 × 130	1.20–1.23
PG 1047	*U*	400	1.20
	B	200	1.18
	V	150	1.19
	I	130	1.19
SA 104	*U*	200, 400	1.15–1.16
	B	90, 200	1.15–1.16
	V	70,150	1.15–1.16
	I	60, 130	1.15–1.16
SA 107	*U*	2 × 200	1.15–1.17
	B	2 × 90	1.16–1.17
	V	2 × 70	1.16–1.17
	I	2 × 60	1.15–1.17

PSF photometry was aperture-corrected using aperture corrections measured on bright, isolated stars across the field.

Aperture photometry was then carried out for all these stars using the PHOTCAL package. We used transformation equations of the following form:

$$u = U - 0.879 \pm 0.007 + 0.45(U - B) - 0.016 \pm 0.010X, \quad (1)$$

$$b = B - 2.081 \pm 0.010 + 0.25(B - V) + 0.132 \pm 0.010X, \quad (2)$$

$$v = V - 2.139 \pm 0.007 + 0.16(B - V) - 0.021 \pm 0.006X, \quad (3)$$

[1] http://www.astro.yale.edu/smarts
[2] http://www.astronomy.ohio-state.edu/Y4KCam/detector.html
[3] http://www.astronomy.ohio-state.edu/Y4KCam/filters.html
[4] IRAF is distributed by the National Optical Astronomy Observatory, which is operated by the Association of Universities for Research in Astronomy, Inc., under cooperative agreement with the National Science Foundation.

$$v = V - 2.159 \pm 0.007 + 0.16(V - I_C) + 0.001 \pm 0.005X, \quad (4)$$

$$i = I_C - 1.136 \pm 0.005 + 0.08(V - I_C) - 0.016 \pm 0.004X, \quad (5)$$

where $UBVI_C$ and *ubvi* are standard and instrumental magnitudes, respectively, and X is the airmass of the observation. We adopted typical values of the extinction coefficients for CTIO (see Baume et al. 2011). To derive V magnitudes, we used equation (3) when the B magnitude was available; otherwise we used equation (4).

World Coordinate System (WCS) header information for each frame was obtained using the ALADIN tool and Two-Micron All-Sky Survey catalogue (2MASS) data (Cutri et al. 2003; Skrutskie et al. 2006). The procedure to perform the astrometric calibration of our data was explained in Baume, Carraro & Momany (2009). This allowed us to obtain a reliable astrometric calibration (∼0.12 arcsec).

We used the Starlink Tables Infrastructure Library Tool Set (STILTS)[5] to manipulate tables and we cross-correlated our $UBVI_C$ and *JHK* 2MASS data. We thus obtained a catalogue with astrometric/photometric information for the detected objects covering a FOV of approximately 20 × 20 arcmin^2 of the cluster region (as in Fig. 1). The full catalogue is made available in electronic form at the Centre de Donnais Stellaire (CDS) website.

2.1 Completeness

To estimate the photometric completeness of our data, we carried out several artificial-star experiments (see Carraro et al. 2005). To this end, we generated 50 new images by adding artificial stars in random positions in the original images, which we then reduced using the same set of parameters. The mentioned 50 new images correspond to the number of experiments for each selected long-exposure passband (V and I) to evaluate the completeness factors (CFs) and their corresponding errors. To preserve the stellar crowding of the original images, the amount of added stars for each experiment was 10 per cent of the total number of stars and followed their colour and luminosity distributions. The CFs were then computed as the ratio between the number of artificial stars recovered by the PSF photometry procedure and the number of artificial stars added. To minimize the error of the computed ratios, we first added the amount of all new stars and the amount of detected ones for all experiments. Out of the 50 experiments per image, we also estimated a completeness error of 0.5 per cent. The whole procedure was applied to estimate the photometric completeness in two areas of the images: one within 5.6 arcmin of the cluster centre, to estimate the cluster completeness, and the other outside this circle, to estimate the field completeness. Values of CF are listed in Table 2 for 0.5-mag bins of V. One can see that there is tendency of the cluster completeness to be lower than the field completeness. This is expected, given the larger crowding of the cluster area. However, the difference is not large and in some cases the completeness values are compatible, within the estimated error. This is probably due to the fact that the cluster is not particularly crowded and is projected towards a rich stellar field.

Table 2. Completeness factors, expressed as percentages, as a function of V magnitude using $\Delta V = 0.5$ bins, inside the circle of 5.6 arcmin radius from the centre and outside this circle. The completeness error is 0.5 per cent.

Magnitude bin	Cluster region	Field region
≤16.75	100.0	100.0
16.75–17.25	96.7	96.9
17.25–17.75	97.9	98.0
17.75–18.25	97.5	97.5
18.25–18.75	97.0	96.8
18.75–19.25	96.5	96.2
19.25–19.75	95.2	95.4
19.75–20.25	90.9	91.9
20.25–20.75	78.4	80.5
20.75–21.25	54.8	57.3
21.25–21.75	28.4	29.2
21.75–22.25	10.8	10.5
22.25–22.75	4.2	4.3
22.75–23.25	2.9	3.2
23.25–23.75	2.5	2.8
23.75–24.25	1.1	1.4

3 SPECTROSCOPIC OBSERVATIONS

We observed red-clump, turn-off (TO) and main-sequence (MS) stars belonging to NGC 4337, using the multi-object, fibre-fed spectroscopy facility Fibre Large Array Multi Element Spectrograph (FLAMES), mounted at the Unit Telescope 2 of the VLT. 113 stars were observed with one single-plate configuration on 2014 March 30, for an integration time of 2775 s. Observations were conducted in combined medusa mode and both the UVES and GIRAFFE spectrographs were employed. Seven red-clump stars were observed with the red arm of UVES, as already reported in Carraro et al. (2014b), while 106 red-clump, TO and MS stars were observed using GIRAFFE. 16 GIRAFFE fibres were allocated to sky position for sky subtraction. UVES and GIRAFFE spectra have a wavelength coverage and resolution of λ = 4760–6840 Å, $R = 47\,000$ (UVES, central wavelength 5800 Å) and λ = 6470–6790 Å, $R = 17\,000$ (GIRAFFE setup HR15N).

Data reduction was performed using the European Southern Observatory (ESO) Common Pipeline Library-based FLAMES–UVES (v.5.3.0) and FLAMES–GIRAFFE (v2.11.1s) pipelines.[6] The GIRAFFE fibres allocated to sky holes were finally median-combined and subtracted from the GIRAFFE stellar spectra. Heliocentric correction was computed using the standard IRAF[7] task *rvcorrect*.

We used the IRAF task *fxcor* to measure the stellar radial velocity (RV) by cross-correlation with synthetic spectra of the Coelho et al. (2005) collection. The synthetic spectra were broadened to the instrumental resolution before cross-correlation. We used synthetic spectra having effective temperatures and surface gravities of $T_{\rm eff} = 4750$ and 6250 K and $\log g = 2.5$ and 4.0 for red-clump and TO, MS stars, respectively. Individual measured radial velocities and the corresponding formal *fxcor* errors are reported in Carraro et al. (2014b) for the stars observed with UVES and all stars have radial velocities consistent with cluster membership. From these seven stars only, with a jackknife bootstrapping technique (Lupton 1993), we derive a mean cluster radial velocity and velocity dispersion of $\langle RV \rangle = -17.76 \pm 0.33$ km s^{-1} and $\sigma = 0.78 \pm 0.61$ km s^{-1}.

[5] http://www.star.bris.ac.uk/∼mbt/stilts/

[6] http://www.eso.org/sci/software/pipelines/

[7] IRAF is distributed by the National Optical Astronomy Observatory, which is operated by the Association of Universities for Research in Astronomy (AURA) under a cooperative agreement with the National Science Foundation.

Table 3. Radial velocities. IDs are from Carraro et al. (2014a). The last column reports the formal *fxcor* error.

ID	V mag	$(V-I)$ mag	RA (2000.0) hh:mm:ss.sss	Dec. (2000.0) dd:mm:ss.ss	RV km s^{-1}	error km s^{-1}
NGC 4337_000169	14.31	0.99	12: 23: 51.895	−58: 10: 58.94	−16.7629	0.787
NGC 4337_000182	14.43	0.90	12: 23: 56.702	−58: 05: 03.12	−15.6799	0.824
NGC 4337_000189	14.47	0.89	12: 24: 06.994	−58: 10: 11.03	−16.8177	1.048
NGC 4337_000197	14.53	0.95	12: 24: 13.800	−58: 07: 53.47	−15.5483	1.106
NGC 4337_000202	14.54	0.90	12: 24: 27.730	−58: 07: 16.07	−18.3345	3.651
NGC 4337_000218	14.61	0.91	12: 23: 28.104	−58: 07: 30.72	−16.2074	0.857
NGC 4337_000256	14.76	0.68	12: 24: 03.012	−58: 06: 50.26	−19.6265	1.083
NGC 4337_000262	14.81	0.94	12: 24: 44.398	−58: 05: 47.11	−15.7375	4.443
NGC 4337_000269	14.85	0.86	12: 24: 06.979	−58: 07: 57.04	−17.2737	3.113
NGC 4337_000283	14.90	0.88	12: 24: 09.497	−58: 07: 51.64	−18.5341	2.503
NGC 4337_000291	14.92	0.85	12: 24: 01.858	−58: 06: 25.27	−20.3456	1.354
NGC 4337_000321	15.02	0.87	12: 23: 43.987	−58: 07: 57.40	−15.7687	1.266
NGC 4337_000329	15.04	0.90	12: 24: 05.244	−58: 06: 42.16	−18.8798	3.374
NGC 4337_000370	15.15	0.87	12: 24: 34.867	−58: 09: 08.68	−14.6227	2.360
NGC 4337_000372	15.16	0.77	12: 24: 00.091	−58: 11: 03.80	−20.8658	1.395
NGC 4337_000433	15.31	0.89	12: 23: 41.124	−58: 09: 58.46	−15.7845	0.812
NGC 4337_000443	15.33	0.88	12: 24: 00.936	−58: 07: 31.91	−18.8097	2.286
NGC 4337_000459	15.38	0.86	12: 24: 04.010	−58: 05: 31.88	−19.1991	1.498
NGC 4337_000460	15.38	0.90	12: 24: 08.304	−58: 09: 34.63	−16.6502	1.188
NGC 4337_000474	15.41	0.91	12: 23: 37.354	−58: 07: 12.47	−18.0435	0.898
NGC 4337_000484	15.44	0.81	12: 23: 50.407	−58: 09: 43.06	−19.0432	1.695
NGC 4337_000539	15.59	0.86	12: 24: 21.283	−58: 07: 39.11	−19.9470	2.048
NGC 4337_000610	15.73	0.89	12: 24: 21.936	−58: 11: 57.95	−20.0636	1.819
NGC 4337_000682	15.89	0.87	12: 23: 34.356	−58: 09: 57.53	−17.1483	0.704
NGC 4337_000694	15.91	0.87	12: 23: 52.399	−58: 10: 15.31	−19.5864	2.160
NGC 4337_000756	16.03	0.92	12: 24: 08.902	−58: 07: 14.45	−16.0065	3.533
NGC 4337_000778	16.07	0.90	12: 24: 31.361	−58: 07: 51.35	−15.6437	2.530
NGC 4337_000839	16.18	0.91	12: 24: 42.842	−58: 09: 14.98	−18.8237	2.170
NGC 4337_000853	16.21	0.95	12: 24: 32.122	−58: 03: 55.80	−16.7957	2.156
NGC 4337_000881	16.25	0.90	12: 24: 08.914	−58: 05: 31.78	−18.6547	3.175
NGC 4337_000918	16.29	0.93	12: 24: 01.690	−58: 05: 35.63	−16.7409	1.717
NGC 4337_001010	16.41	0.94	12: 23: 57.686	−58: 04: 54.88	−19.9451	2.400
NGC 4337_001058	16.48	0.97	12: 24: 21.312	−58: 08: 10.18	−18.8888	3.001
NGC 4337_001090	16.51	0.96	12: 23: 46.778	−58: 09: 39.53	−19.7798	2.552
NGC 4337_001108	16.54	0.95	12: 24: 28.673	−58: 05: 58.85	−20.4966	3.097
NGC 4337_001210	16.68	0.97	12: 23: 37.944	−58: 10: 32.02	−15.6153	1.449
NGC 4337_001264	16.74	1.00	12: 24: 19.078	−58: 02: 55.32	−17.5050	2.688
NGC 4337_001271	16.75	0.95	12: 24: 00.290	−58: 05: 01.61	−17.1769	2.417
NGC 4337_001301	16.78	1.01	12: 23: 43.613	−58: 12: 26.68	−18.1352	1.736
NGC 4337_001403	16.90	0.99	12: 23: 23.040	−58: 06: 35.75	−16.7813	3.057
NGC 4337_001408	16.91	0.99	12: 23: 36.566	−58: 08: 20.33	−18.9967	2.245
NGC 4337_001461	16.96	1.01	12: 23: 39.266	−58: 06: 56.66	−16.6959	4.066
NGC 4337_100110	13.91	1.32	12: 23: 57.209	−58: 07: 14.45	−16.1309	0.554
NGC 4337_100124	14.02	1.32	12: 24: 31.786	−58: 08: 02.11	−17.6769	0.544
NGC 4337_100130	14.06	1.36	12: 24: 04.898	−58: 05: 09.85	−18.2653	0.500

The GIRAFFE sample includes four stars selected in the red-clump colour–magnitude diagram (CMD) region and 102 stars in the TO, MS region. Given the expected significant field contamination in the TO, MS region of the CMD, in order to select likely cluster members we selected stars with formal error from the *fxcor* fit lower than 5 km s^{-1} and we applied a 2σ clipping rejection to this sample. With this selection, we ended up with 45 likely cluster members (see Table 3).

To make our selection more solid and convincing, we show a multi-panel plot in Fig. 2. In the bottom left panel, the target stars observed with GIRAFFE (symbols) are plotted on top of the V versus $V-I$ CMD of NGC 4337 (dots). Stars used in the calculation of the cluster mean radial velocity and velocity dispersion (see text) are marked as filled triangles, while large open circles are stars excluded by the above selection. In the top left panel, the formal error in the radial velocity measured with the favour cross-correlation task is plotted against the stellar V magnitude. The expected trend of larger error with fainter magnitudes is evident. The cut applied at errors larger than 5 km s^{-1} is shown as a continuous line. The dotted line represents a possible alternative selection of errors, which would retain stars in the lower envelope described by the distribution. Four additional stars would be excluded by this selection (see below). In the bottom right panel, we show the measured radial velocities against the distance from the cluster centre, adopted as (RA, Dec.) = (186.°0, −58.°123). The vertical dashed lines are 2σ limits from the cluster mean, after applying a 2σ-clipping rejection. Open circles in the region delimited by the two dashed lines are stars excluded from the selection due to their RV errors, larger than 5 km s^{-1}. The middle right panel shows the measured radial velocities against the stellar V magnitude. Finally, the top right panel

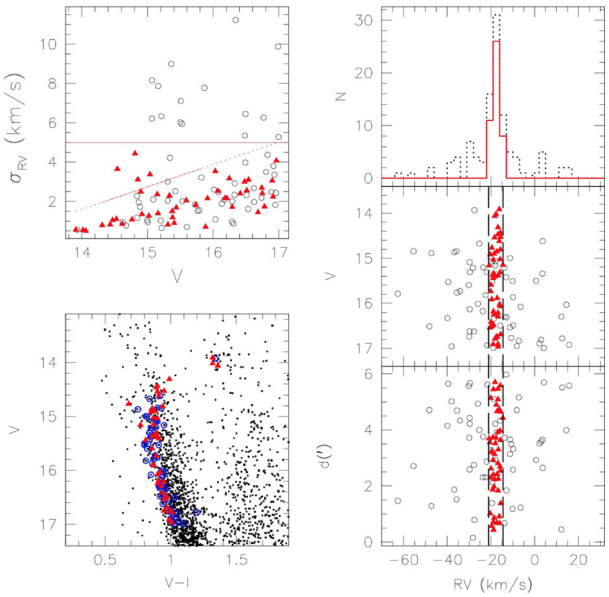

Figure 2. Spectroscopic membership assessment. See text for details.

shows histograms of all the radial velocities (dotted line) measured from GIRAFFE spectra and the radial velocities of the stars retained above as radial velocity members (continuous line) for calculating the cluster mean radial velocity and velocity dispersion.

With the help of this figure, we can argue that the lower envelope of the mean trend reaches about 5 km s^{-1} at $V = 17$, which is the faintest magnitude we reached. There are, however, several outliers with respect to the mean trend. Most of them are excluded with the cut in error we applied.

A perhaps better-motivated selection would apply a cut in RV error that scales with magnitude. We found that a proper relation would be to accept stars having RV errors lower than

$$\mathrm{err}(RV) < 1.14 \times V - 14.36.$$

By applying this criterion, four additional stars are excluded before applying the 2σ clipping procedure at a magnitude in range $V = 14.5$–15.5. These four stars, however, have errors lower than 5 km s^{-1} and are not so evidently discrepant from the bulk of the mean trend. With this new selection, we would retain 41 stars and obtain

$$\langle RV \rangle = -17.80 \pm 0.26\,\mathrm{km\,s^{-1}}, \qquad \sigma = 1.67 \pm 0.13\,\mathrm{km\,s^{-1}},$$

which is totally consistent with applying the cut on errors at 5 km s^{-1}. Finally, if a cut on the formal *fxcor* error is not applied before the 2σ clipping procedure, we end up retaining 53 stars and obtaining

$$\langle RV \rangle = -17.93 \pm 0.21\,\mathrm{km\,s^{-1}}, \qquad \sigma = 1.54 \pm 0.10\,\mathrm{km\,s^{-1}}.$$

We believe, therefore, that using the formal *fxcor* is a good choice and we will use the original 45 members in the remainder of the article.

By applying the jackknife resampling technique again, we finally obtain a mean cluster radial velocity and velocity dispersion of $\langle RV \rangle = -17.78 \pm 0.28$ km s^{-1} and $\sigma = 1.64 \pm 0.13$ km s^{-1}. These values are formally consistent (within 2σ) with the results from the UVES sample (Carraro et al. 2014b). While the mean cluster radial velocity is practically identical for the two samples, the radial velocity dispersion obtained from the GIRAFFE sample is

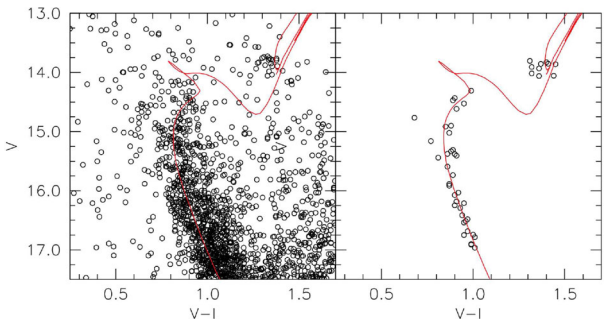

Figure 3. Distance determination. The left panel shows all the stars detected in v and I, while the right panel shows RV members only. The isochrone is for an age of 1.5 Gyr and a metallicity $Z = 0.025$.

significantly larger and seemingly with a smaller error. The UVES sample is, however, significantly smaller in size (7 against 45 stars). We will consider in the following the velocity dispersion derived from GIRAFFE as representative of the cluster dispersion. The full table with all 113 radial velocity measurements will be made available electronically.

4 CLUSTER DISTANCE

The distance to NGC 4337 is essential to derive the cluster linear radius and to convert light into mass. In Carraro et al. (2014b), it was established that the cluster is metal-rich, with [Fe/H] $= +0.12 \pm 0.05$ and with an age of 1.6 ± 0.1 Gyr. Here, we refine the cluster distance and reddening by fitting the CMD of NGC 4337 using the radial velocity members only (see Table 3). This is shown in Fig. 3. The cluster MS for members only is very clearly defined, with the typical curvature of an intermediate-age cluster in the TO region. The TO is located at $V = 15$ mag. A clump spread in colour is located at mean magnitude $V = 13.9$. Two stars bluer than $(V - I) \sim 0.8$ mag could be cluster blue stragglers.

We find that an isochrone of 1.5 Gyr (Bressan et al. 2012) reproduces the shape of the TO and the magnitude of the clump better, than an isochrone of 1.6 Gyr. This convincing fit yields a reddening $E(V - I) = 0.385 \pm 0.005$ and an apparent visual distance modulus $(m - M)_V = 12.72 \pm 0.02$ mag, where uncertainties are estimated by visual inspection. In other words, we eyeballed the location of the isochrone with respect to the member stars by displacing it along the vertical and horizontal directions iteratively, until an acceptable fit could not be found. This implies that the cluster distance is 2.2 ± 0.1 kpc from the Sun, slightly lower than the Carraro et al. (2014b) estimate.

5 SURFACE DENSITY MAPS AND CLUSTER CENTRE

To determine the coordinates of the cluster centre and to study the cluster two-dimensional (2D) structure, we derived surface density maps (2D density distributions) by using a kernel estimator (see for example, Seleznev et al. (2010) and Carraro & Seleznev (2012) and the detailed description of this method in Silverman (1986)). Density maps were derived by varying the limiting magnitude. We warn the reader that star counts cannot be computed in a strip a kernel half-width h wide close to the border of the field, to prevent undersampling.

Fig. 4 (left panel) shows the surface density map, centred at RA $= 12^{\mathrm{h}}24^{\mathrm{m}}04^{\mathrm{s}}$, Dec. $= -58^{\circ}07'24''$. Both x and y coordinates are in

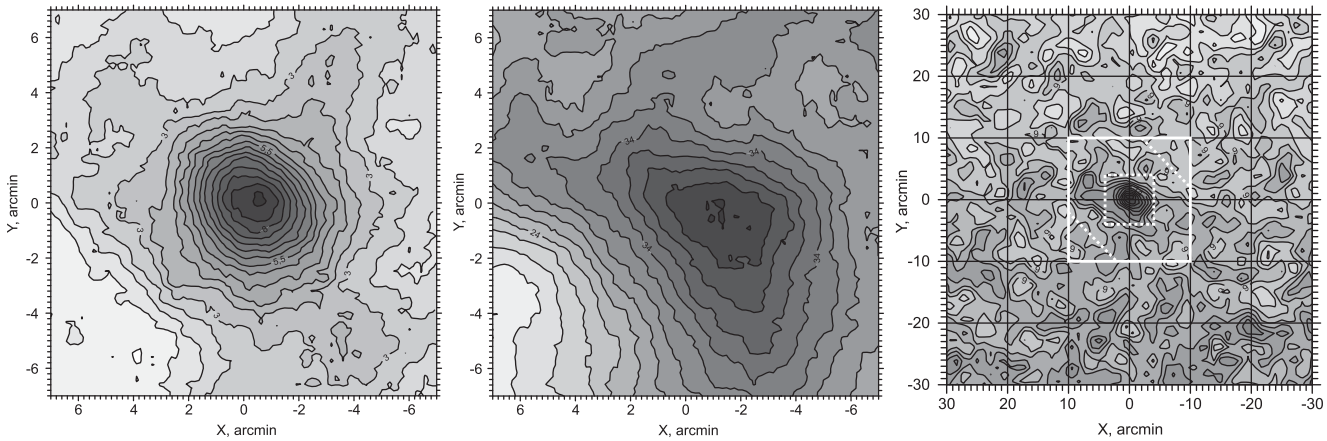

Figure 4. *Left*: map of surface density of the cluster for stars with $V \leq 16$ mag. The density units are arcmin^{-2}. *Middle panel*: map of surface density of the cluster with stars having $V \leq 20$ mag. *Right*: map of surface density of the cluster with stars having $J \leq 16$ mag and derived from 2MASS. The rectangle of white solid lines shows the field covered by our optical data. The rectangle of white dotted lines shows the cluster field for luminosity function (LF) derivation, while the white dotted lines in the corners of the white-solid-line rectangle show the comparison field for LF derivation.

arcmin, with x increasing towards the east and y towards the north. Only stars with $V \leq 16$ mag are considered and we adopted 3 arcmin as the kernel half-width. Density units are arcmin^{-2} and density values are shown at contour lines. This map was chosen as the best representation of the cluster star distribution, taking into account the CMD and with the sole purpose of deriving an estimate of the cluster centre. The cluster centre position was determined in two ways. First, the contour line corresponding to a density value of 7 arcmin^{-2} was approximated with an ellipse in polar coordinates, following Pancino et al. (2003). Then the centre position was determined as the mean value of the coordinates of the contour line in 30° intervals of position angle. Secondly, the centre coordinates were determined as x and y coordinates of the maxima of the corresponding linear density functions, obtained by kernel estimation with values of kernel half-width of 1 and 3 arcmin. The mean coordinates of the cluster centre by both methods are $x = -0.34 \pm 0.15$ arcmin and $y = 0.02 \pm 0.13$ arcmin. Finally, the cluster centre was adopted as RA = 186.°00594, Dec. = −58.°12300, with an uncertainty of about 10 arcsec. The robustness of this centre position was confirmed by radial surface density profiles (see below; if the centre location is determined incorrectly, the density profile can have a minimum at the centre).

The middle panel in Fig. 4 shows a surface density map with the same parameters as in the left panel, but for fainter stars ($V \leq 20$ mag). The cluster appears to be stretched from north-east to south-west. This distortion is supported by the surface density map derived with the same method using 2MASS data and shown in the right panel. For this case, the adopted kernel half-width is 2 arcmin and the limiting magnitude $J = 16$ mag. Elongation of an open cluster can arise, for example, due to tidal action of the Galaxy. It was studied in numerical experiments (see for example, Kharchenko et al. 2009; Chumak et al. 2010) and revealed in real clusters (see for example, Davenport & Sandquist 2010). Thus, we have every reason to consider stars forming elongations of NGC 4337 as possible cluster members. The white box in the right panel of Fig. 4 indicates the field covered by our optical photometry. Due to the elongated shape of the cluster, the only possible regions for estimating the field density are in the north-west and south-east corners of this field. We remind the reader that these field regions are necessary for deriving the luminosity function of the cluster and its mass, as discussed in the following.

6 RADIAL DENSITY PROFILES AND CLUSTER MASS

The cluster radial surface density profiles $F(r)$ were derived using the cluster centre coordinates obtained in the previous section and for different limiting magnitudes $V_{\rm lim}$. The kernel estimator method was used (Merritt & Tremblay 1994; Seleznev 2016). The density profile for stars with $V_{\rm lim} = 16$ mag is shown in the left panel of Fig. 5. The maximum distance from the centre is taken as one kernel half-width from the detector border to avoid undersampling (see previous section). We estimated the kernel half-width empirically by comparing density profiles with different kernel half-widths and selecting the smoothest curve, which closely follows the mean trend defined by curves with much smaller kernel half-width values (Merritt & Tremblay 1994; Seleznev 2016). The density profile is shown with a solid line, while the border of the 2σ width confidence interval is shown with two dotted lines. This interval was obtained by employing the smoothed bootstrap estimate method (Merritt & Tremblay 1994; Seleznev 2016). The visual estimate of the field stellar density is indicated with a straight solid line and was inferred as follows: if the density profile gets flat within the covered region (this is the case for NGC 4337), then the field density line is drawn in such a way that the fluctuations around it have equal areas. Seleznev (2016) showed that the visual estimate of the field density correlates well with the result of its determination with a much more sophisticated method. As a consequence, the cluster radius corresponds to the intersection of the density profile with the field density level. The associated uncertainty is computed using the intersections of the confidence interval lines with the field density at the cluster radius location. Seleznev (2016) showed that this estimate of cluster radius does not depend significantly on the adopted kernel half-width value, when the adopted kernel half-width and smaller values are used. The uncertainty in the field density estimate was evaluated as half of the confidence interval width at the cluster radius point.

The cluster radius $R_{\rm c}$ is considered here as the radius of the sphere around the cluster centre where the cluster differs from the field (Danilov, Matkin & Pylskaya 1985; Danilov & Seleznev 1994). This value does not coincide with the tidal radius. The latter can be larger than $R_{\rm c}$ (for example, if field density fluctuations prevent detection of the outer low-density part of the cluster) or smaller

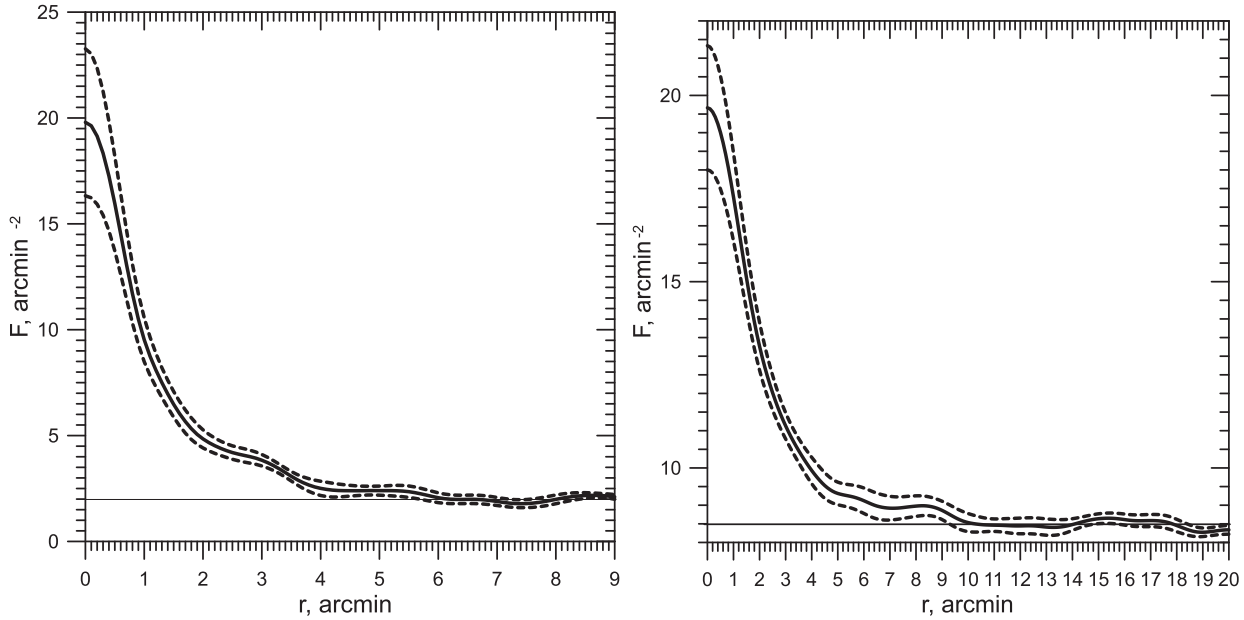

Figure 5. *Left*: radial surface density profile of the cluster for $V_{\rm lim} = 16$ mag. *Right*: radial surface density profile of the cluster with stars of $J_{\rm lim} = 16$ mag, obtained with the data of 2MASS. The solid line shows the density profile obtained by a kernel estimator with kernel half-width of 3 arcmin for the left panel and 2 arcmin for the right panel. The dashed lines show the 2σ width confidence interval. The straight solid line shows the value of field surface density determined with the density profiles.

Table 4. Cluster parameters with different limiting magnitudes.

$V_{\rm lim}$	$R_{\rm c}$ arcmin	$R_{\rm c}$ pc	$F_{\rm b}$ arcmin^{-2}	$N_{\rm c}$	$r_{\rm h}$ arcmin
14	4.6 ± 0.3	2.9 ± 0.2	0.30 ± 0.09	33 ± 19	2.0 ± 1.4
15	6.7 ± 0.7	4.3 ± 0.4	0.66 ± 0.16	117 ± 53	2.3 ± 1.1
16	6.2 ± 0.5	4.0 ± 0.3	1.68 ± 0.26	198 ± 72	2.4 ± 0.9
17	7.0 ± 0.2	4.5 ± 0.1	3.0 ± 0.4	392 ± 122	3.2 ± 1.0
18	7.2 ± 0.2	4.6 ± 0.1	5.5 ± 0.6	650 ± 177	3.7 ± 1.0
19	6.7 ± 0.4	4.3 ± 0.3	11.5 ± 0.8	758 ± 218	3.4 ± 0.9
20	6.5 ± 0.3	4.2 ± 0.2	22.0 ± 1.1	1128 ± 280	3.7 ± 0.6
21	7.0 ± 0.2	4.5 ± 0.1	35.6 ± 1.4	1931 ± 395	4.3 ± 0.6

than $R_{\rm c}$ (for example, if we detect the relatively dense part of the cluster tidal tail). We do not fit radial surface density profiles with the King model, because it does not reproduce the outer part of open clusters well, leading to underestimation of open cluster size (Seleznev 2016).

The use of radial density profiles implies an assumption of spherical symmetry. What effect does this assumption have on our results? Open clusters are often asymmetric (NGC 4337 is just such a case). The cluster radius obtained with the radial density profile corresponds in that case to the distance from the cluster centre to the most remote point of the cluster boundary (if background density fluctuations are not too large). Points of the density profile represent azimuthally averaged values of density. Then the integral of the radial density profile will give the same result as the integral of the two-dimensional density distribution. This is important for the following treatment.

Estimates of cluster radius for different limiting magnitudes are listed in the second column of Table 4. The third column contains the cluster radius in pc, adopting the distance as in Section 5. The size of field under investigation is relatively small and there is a possibility that we are missing the cluster halo. Therefore it is more conservative to consider these values as lower estimates of the cluster radius. The surface density profile derived using 2MASS (Fig. 5, right panel) lends further support to this scenario. In fact, the cluster radius can be estimated in this case to be as large as $R_{\rm c} = 10.0 \pm 0.8$ arcmin. A visual comparison with the density maps in Fig. 4 shows that this radius estimate corresponds to the cluster's maximum elongation in the north-east and south-west directions. In the perpendicular direction, the cluster extent seems considerably smaller. Due to this, we use the mean field star surface density $F_{\rm b}$ (fourth column of Table 4) as determined for the triangles marked by the white dotted line in the right panel of Fig. 4. It was obtained with the cumulative luminosity function for these regions.

Finally, one can notice from Table 4 that the brightest stars of NGC 4337 (the red giant branch (RGB) clump stars) are distributed in a smaller volume than fainter stars, which indicates that the cluster has already experienced some dynamical evolution and mass segregation.

We integrated the density profile to estimate the cluster star number and the parameter $r_{\rm h}$, namely the radius of the circle around the cluster centre that contains half of the cluster stars. Integration was performed using the Simpson method with an accuracy estimate, while the interpolation of density profiles was performed by using a spline function. The fifth column of Table 4 reports the cluster star number, while the sixth column contains estimates of $r_{\rm h}$ and indicates that this increases on increasing the limiting magnitude. Usually, in the literature, $r_{\rm h}$ is defined as the half-light or -mass radius, which does not necessarily coincide with the radius at which half of the stars are counted. Nevertheless $r_{\rm h}$ is used for the virial mass estimate of star cluster, while the accurate formula for the virial mass contains the mean inverse star-to-star distance instead of $r_{\rm h}$. Therefore it is not very important how $r_{\rm h}$ is determined.

The number of cluster stars can be used to infer an estimate of the cluster mass, as illustrated in Table 5. The first column contains the magnitude V and the second column lists the absolute magnitude $M_{\rm V}$, calculated adopting the distance modulus derived in Section 5. The third column contains the star mass corresponding

Table 5. Cluster mass estimate.

V	M_V mag	m $M_\odot$	$\langle m_i \rangle$ $M_\odot$	N_i	$\mathfrak{M}_i$ $M_\odot$
14	1.28 ± 0.02	1.90 ± 0.00	1.95 ± 0.00	33 ± 19	64 ± 37
15	2.28 ± 0.02	1.66 ± 0.01	1.78 ± 0.00	84 ± 56	150 ± 100
16	3.28 ± 0.02	1.39 ± 0.01	1.53 ± 0.01	81 ± 89	124 ± 136
17	4.28 ± 0.02	1.17 ± 0.01	1.28 ± 0.01	194 ± 142	248 ± 182
18	5.28 ± 0.02	1.00 ± 0.00	1.09 ± 0.01	258 ± 215	281 ± 234
19	6.28 ± 0.02	0.86 ± 0.01	0.93 ± 0.01	108 ± 281	100 ± 261
20	7.28 ± 0.02	0.74 ± 0.00	0.80 ± 0.01	370 ± 355	296 ± 284
21	8.28 ± 0.02	0.63 ± 0.00	0.69 ± 0.00	803 ± 484	554 ± 334

to this magnitude, taken from the table of isochrones for the age and metallicity of NGC 4337 (Carraro et al. 2014b; Bressan et al. 2012). The fourth column contains the mean mass of the magnitude interval between this magnitude and the magnitude from the previous row (the mean mass value in the first row is for brighter – RGB clump – cluster stars). The fifth column lists the number of stars in this magnitude interval and the sixth column contains the mass estimate of cluster stars from the same magnitude interval.

We anticipate here that the cluster luminosity function (see below) will show a sharp decrease beyond $V \simeq 21$ mag, despite completeness correction. This cut-off is most probably produced by the large uncertainty in the completeness factor at magnitudes close to the investigation limit and by selection effects. Because of this, the cluster mass was estimated only down to $V = 21$ mag, resulting in $\mathfrak{M} = 1820 \pm 620\,M_\odot$. This is clearly intended as a lower estimate of the cluster actual mass, because the mass of $0.63\,M_\odot$ is far from the lower stellar mass limit and the cluster radius values in Table 4 are lower estimates (see above).

7 THE CLUSTER LUMINOSITY FUNCTION

The same kernel estimator method was employed to construct the cluster luminosity function (LF: see e.g. Prisinzano et al. 2001). However, at odds with Prisinzano et al. (2001), we adopt here a fixed (not adaptive) kernel, which is more effective in the presence of the rich stellar field around NGC 4337, since it gives the same result with less computational effort.

We estimated the LF in the cluster area (central rectangle, marked by white dotted line in Fig. 4, right panel) and in the comparison region (two triangles in the corners between the white dotted lines and the boundary, marked by a white solid line). Due to the elongated shape of NGC 4337, we expect that these two regions do not contain cluster stars and effectively represent the stellar field in the cluster vicinity. It is worth noticing that the area of the cluster region is equal to the area of the comparison fields and that we took the results of incompleteness analysis into account.

The LF of the cluster stars was then derived as the difference between the LFs of the cluster region (Fig. 6, left panel) and the comparison region (Fig. 6, middle panel). This LF is shown in the right panel of Fig. 6 with a thick solid line, while thin solid lines indicates the 2σ width confidence interval. The kernel half-width was taken to be 0.5 mag, which was chosen by the same consideration as in the case of the density profiles (see above in Section 6). The kernel estimate is a continuous and differentiable function and it is very important for further mass function evaluation (Seleznev 2016).

One can notice that, below $V = 21$ mag, the LF of cluster stars shows a sharp decrease, despite completeness correction. The most probable explanation is that the completeness factors have large uncertainties near the investigation limit and we have reached the completeness limit of our photometric data set (see Table 2). In the following, we therefore restrict ourselves to stars brighter than $V = 21$ mag. The CMD (Fig. 3) shows that the brightest cluster stars have magnitudes in the interval $V \in [13.5; 14.3]$ mag and therefore $V = 13$ mag seems quite a reasonable magnitude to start the LF computation with. Negative values of LF are not impossible, because this was obtained as a difference between two distributions. The negative LF regions (near $V = 12.5$ and $V = 22$ mag) are in any case outside the region of interest to us. Finally, we draw attention to a LF minimum near $V = 16$ and $V = 18$ mag. We run a Kolmogorov–Smirnov (KS) test that does not show that these minima are statistically significant, but the chi-square test shows noticeable difference, with a p-value of about 0.17. Comparison of the LF (and its histogram in the case of the chi-square test) was carried out with curves (and histograms) where the minima were replaced by the graduate positive slope. In the case of the KS test, a cumulative LF was constructed.

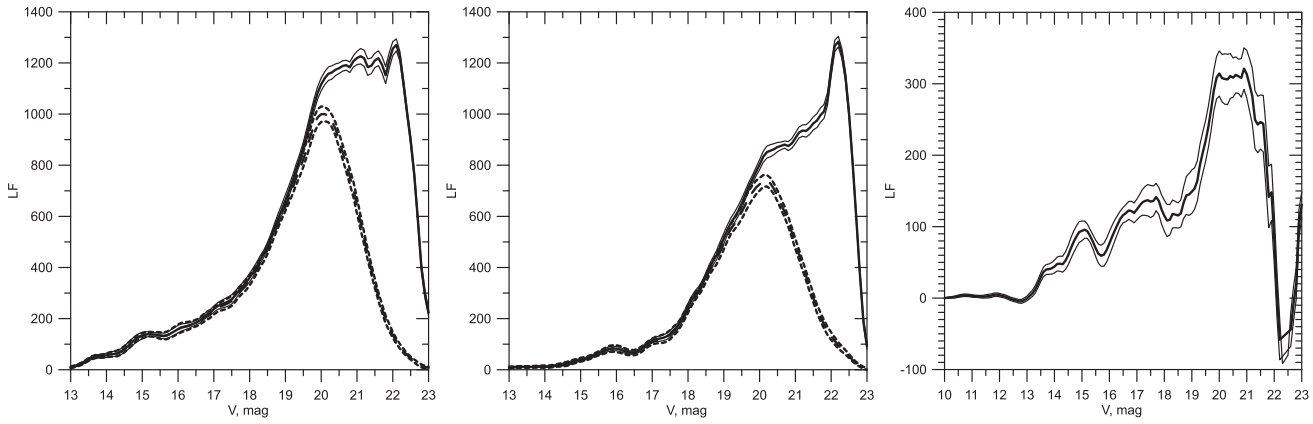

Figure 6. The luminosity function of NGC 4337. *Left*: the thick solid line shows the LF for the cluster region (white-dotted square in Fig. 4, right panel), corrected for incompleteness. The LF was obtained by a kernel estimator with kernel half-width of 0.5 mag. Thin solid lines show the 2σ width confidence interval. Dashed lines show the uncorrected LF for this region with its confidence interval. *Middle*: the same as in the left panel, but for the field region (triangles separated by white dotted lines in Fig. 4, right panel). *Right*: the LF for cluster stars, the result of subtraction of the field LF (thick solid line in the middle panel) from the cluster region LF (thick solid line in the left panel), with its 2σ confidence interval.

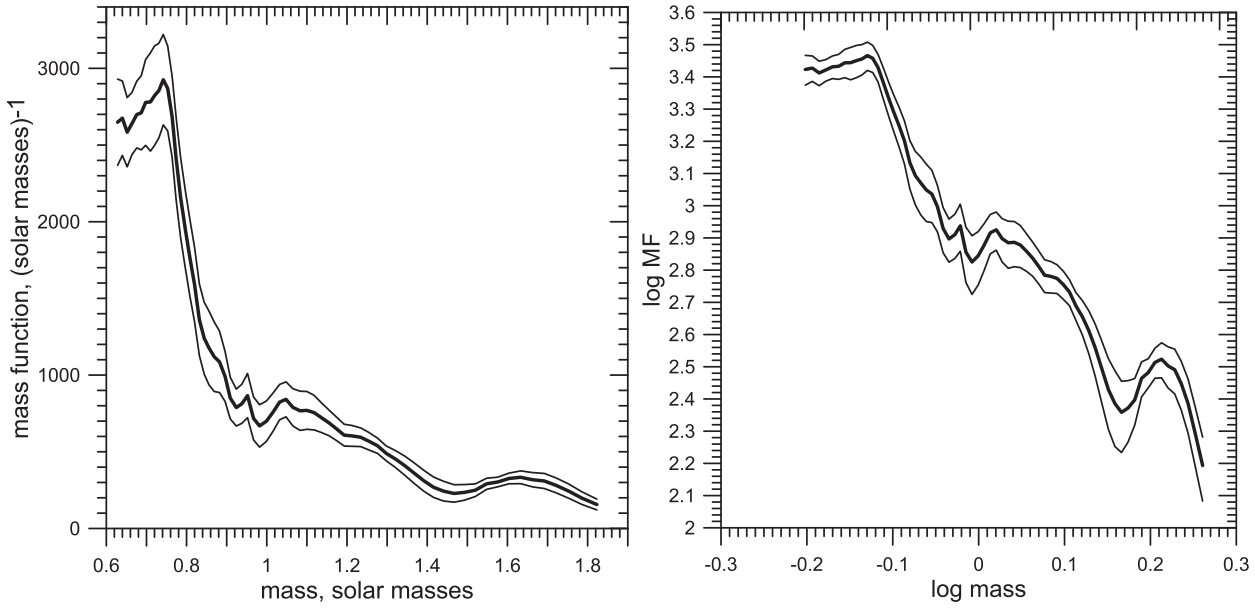

Figure 7. *Left*: mass function (MF) of the cluster. The thick solid line shows the MF, thin solid lines show the 2σ width confidence interval. *Right*: mass function of the cluster in logarithmic form. Symbols are the same as in the left panel.

It is crucial to underline that this LF is normalized to the cluster star number inside the white-dotted-line rectangle (see right panel in Fig. 4). In order to obtain a normalization to the whole cluster, we need to derive the ratio of the cluster star number inside the rectangle to the total cluster star number. The cluster star number inside the rectangle was derived as the double integral of the surface density profile over the rectangle and integration was performed with the method of rectangles in two dimensions. Then the field star number was subtracted from the result of this integration. The total star number and the surface density of field stars were both taken from Table 4. The normalization ratio was then determined for limiting magnitude $V_{\rm lim} = 21$ mag to be 0.55 ± 0.24.

8 THE CLUSTER MASS FUNCTION

Let consider the cluster mass function (MF) $\psi(m)$ as

$$\psi(m) = \frac{{\rm d}n}{{\rm d}m}, \qquad \int_{m_1}^{m_2} \psi(m)\,{\rm d}m = N, \tag{6}$$

where m is the mass of a star and N is the number of cluster stars in the mass range $[m_1; m_2]$. The cluster mass $\mathfrak{M}$ for this mass range is then determined as

$$\int_{m_1}^{m_2} \psi(m) m\,{\rm d}m = \mathfrak{M}. \tag{7}$$

Using the same terminology, the luminosity function can be written as

$$\varphi(V) = \frac{{\rm d}n}{{\rm d}V}, \qquad \int_{V_1}^{V_2} \varphi(V)\,{\rm d}V = N. \tag{8}$$

If the mass range corresponds to the magnitude range, the cluster star number N will be the same.

Let $m = m(V)$ be the stellar mass–luminosity relation. In this case, we have

$${\rm d}m = \frac{{\rm d}m}{{\rm d}V} \cdot {\rm d}V \equiv m'_V \cdot {\rm d}V \qquad \text{and} \tag{9}$$

$$\psi(m) = \frac{{\rm d}n}{{\rm d}m} = \frac{{\rm d}n}{|m'_V| \cdot {\rm d}V} = \frac{\varphi(V)}{|m'_V|}. \tag{10}$$

The LF was converted into a MF in the magnitude range $V \in [14.5; 21]$ mag, which corresponds to the absolute magnitude range $M_{\rm V} \in [1.78; 8.28]$ mag. This ensures we avoid any ambiguity in the region of RGB clump stars and selection effects in the region $V > 21$ mag. The relation $m = m(V)$ was taken from the Padova suite of models (Bressan et al. 2012) and was approximated by a spline function, together with its first derivative. The cluster mass function is shown in Fig. 7 (left panel) in linear form and in Fig. 7 (right panel) in logarithmic form.

A least-squares regression over the logarithmic MF yields a MF slope of -2.68 ± 0.08 (in this scale the standard Salpeter slope is -2.35). In order to take into account the confidence interval for the MF, numerical experiments have been performed. For every m points, the value of MF was randomly taken from the interval $[MF - 3\sigma; MF + 3\sigma]$ according to a Gaussian distribution with its centre at the MF value. Then a linear regression was performed with an even series of MF values. The error of the argument (the mass) was not taken into account. 20 experiments produced a mean slope of -2.72 ± 0.08, virtually identical to the values obtained by simple linear regression.

A lower estimate of the cluster mass was then derived by integrating the MF over the whole mass range. This yielded a mass of $976 \pm 135\,{\rm M}_\odot$ for stars inside the white-dotted-line rectangle in Fig. 4 (right panel) and in the magnitude range $V \in [14.5; 21]$ mag. Assuming the same MF for the entire cluster, the lower estimate of total cluster mass in the same magnitude range would be $1775 \pm 812\,{\rm M}_\odot$ (the normalization ratio from the previous section is applied). If, in addition, we account for stars with $V \leq 14.5$ mag from the surface density profile for stars with $V_{\rm lim} = 14.5$ mag, this estimate would become $1880 \pm 820\,{\rm M}_\odot$. Notice that the possible

(small) bias towards high luminosities (masses) in our LF sample, caused by dynamical mass segregation, implies that the above mass estimate should be considered as an upper limit.

The reader can see that this mass estimate does not differ significantly from the estimate obtained by surface density profiles in the previous section, $\mathfrak{M} = 1820 \pm 620\,\mathrm{M}_\odot$ (see above). Both estimates are in any case still a lower limit for the mass estimate, because of the unknown low-mass end of the stellar mass distribution and the unaccounted-for unresolved binaries and probable remnants of massive stars.

9 CLUSTER DYNAMICAL MASS

9.1 Isolated cluster

The most common, but rough, way to obtain a cluster dynamical mass estimate is by means of the computation of the 1D (radial) velocity dispersion for a set of n stars for which the radial velocity is available. This gives

$$\sigma_\mathrm{r}^2 = \frac{\sum_{i=1}^{n} \left(v_{\mathrm{r},i} - \langle v_\mathrm{r}\rangle\right)^2}{n}, \tag{11}$$

where $\langle v_\mathrm{r}\rangle$ is the mean radial velocity, which corresponds to the cluster sampling systemic velocity. In the case of NGC 4337, data in Table 3 give $\langle v_\mathrm{r}\rangle = -17.78 \pm 1.00$ kms^{-1} and $\sigma_\mathrm{r} = 1.62 \pm 0.30$ kms^{-1}. The virial mass is obtained as

$$M = \frac{R\sigma^2}{\alpha G}, \tag{12}$$

where σ is the 3D velocity dispersion, which, in the assumption of an isotropic velocity distribution, is $\sigma^2 = 3\sigma_\mathrm{r}^2$, R is the cluster radius and α is a geometric factor such that $\Omega = -\alpha GM^2/R$, with Ω the cluster gravitational energy. Applying equation (7) to our data, we obtain $5.26 \times 10^3\alpha^{-1} \leq M(\mathrm{M}_\odot) \leq 8.34 \times 10^3\alpha^{-1}$, adopting the minimum (2.9 pc) and maximum (4.5 pc) value for R in Table 4.

The choice of $\alpha = 3/5$ (homogeneous cluster) gives $8.77 \times 10^3 \leq M(\mathrm{M}_\odot) \leq 1.93 \times 10^4$, while a factor of 2 larger α (much more compact cluster) leads to $4.39 \times 10^3 \leq M(\mathrm{M}_\odot) \leq 9.65 \times 10^3$, all values significantly larger than the estimates based on the radial density profile in Section 6, 1820 $\mathrm{M}_\odot$, or on the cluster MF in Section 8, 1880 $\mathrm{M}_\odot$.

Actually, the ratio between the dynamical mass estimate and the density profile or LF-based estimates is in the range 2.34–10.63, which indicates either a very large quantity of invisible mass or that the cluster is not virialized.

What we said above suggests it is important to deepen the topic of dynamical mass estimates. In this regard, we developed a simple formula based on the knowledge of a limited sample of n angular positions and radial velocities, as follows. The 1D kinetic energy in the cluster rest frame is straightforwardly obtained as

$$K_1 = \frac{1}{2}\sum_{i=1}^{n} m_i(v_{\mathrm{r},i} - \langle v_\mathrm{r}\rangle)^2, \tag{13}$$

while the gravitational potential energy is

$$\Omega = -\sum_{j>i} G\frac{m_i m_j}{r_{ij}}, \tag{14}$$

where $r_{ij} \equiv |\boldsymbol{r}_i - \boldsymbol{r}_j|$ is the distance between the ith and jth star in the system, the position vectors of which are $\boldsymbol{r}_i$ and $\boldsymbol{r}_j$, with r_i and r_j their moduli. Given the angular coordinates (right ascension and declination, hereafter θ and ϕ) of the stars, we have

$$r_{ij} = \sqrt{r_i^2 + r_j^2 - 2r_i r_j\left[\cos\phi_i\cos\phi_j + \sin\phi_i\sin\phi_j\cos(\theta_i - \theta_j)\right]}. \tag{15}$$

The assumption that the generic star distance to the reference frame origin, r_i, is the same (the cluster distance, d) leads to

$$r_{ij} = \sqrt{2}d\sqrt{1 - \left[\cos\phi_i\cos\phi_j + \sin\phi_i\sin\phi_j\cos(\theta_i - \theta_j)\right]}. \tag{16}$$

The pair distances computed with equation (16) are underestimated, so a better approximation, once the cluster size R is known, is to insert in equation (15) r_i and r_j randomly sampled within the cluster radius, via the simple linear expression

$$r_i = d - R + 2Rt, \tag{17}$$

where t is a random variable in the [0, 1] interval.

We computed the cluster potential energy, which we call Ω_3, using the latter approximation for the pair distances, while for the kinetic energy we adopted the natural assumption of velocity isotropy, which leads to a 3D kinetic energy for the n star sample that is simply $K_3 = 3K_1$.

Note that although we took into account, in an approximate way, the 3D structure of the cluster, the virial ratio obtained, $Q_3 = 2K_3/|\Omega_3|$, is expected to be an overestimate of the actual virial ratio even in the absence of non-luminous matter, because the sample kinetic energy is $\mathcal{O}(n/N)$ of the total cluster kinetic energy, while the gravitational energy scales quadratically, so that $\Omega^{(n)} \propto (n/N)^2\Omega^{(N)}$ (N is here the total number of cluster stars).

Given this, a better estimate than equation (12) for the virial mass is the mass that *closes* the cluster gravitationally:

$$M_3 = Q_3 M_*, \tag{18}$$

where $M_* = 68.52\,\mathrm{M}_\odot$ is the mass of the 45 member stars for which radial velocities and angular coordinates are given in Table 3. Note that the value of M_* is about 3.7 per cent of the mass evaluated by the surface density profile (Section 6) and via the luminosity function in Section 8. Adopting the error propagation formula giving the safest error estimate, we get $M_3 = 11400 \pm 4550\,\mathrm{M}_\odot$. This error does not include error propagation due to uncertainty in the star radial velocities, distances and angular coordinates.

An important question to answer is this: can the low-mass, faint stars of the cluster and high-mass remnants account for the huge difference between this virial mass and the masses estimated via the density profile and the MF of previous sections? The answer to this question comes from evaluation of the quantity of mass accounted for by the power-law mass function of Section 8, $\psi(m) \propto m^{-s}$, where s was taken at nominal values of -2.68 and -2.72, cutting the MF at the lowest value $m_\mathrm{min} = 0.1\,\mathrm{M}_\odot$ (roughly the brown dwarf limit) and $m_\mathrm{max} = 25\,\mathrm{M}_\odot$. Note that the precise assumption regarding m_max is not relevant because of the rapid decrease of the MF for large mass values. The magnitude interval of visible stars is [1.78; 8.28] mag, which transforms into the [0.63; 1.78] $\mathrm{M}_\odot$ mass interval. In Table 6, we report the values of the mass contributed by the cluster stars outside this mass interval (low-mass, index 'l', and high-mass, index 'h') and the mass given by visible stars. Values in this table essentially show how dark stars (in the low- and high-mass tail of the MF) can marginally provide the undetected mass to give a virialized cluster without claiming for dark matter. In this regard, we additionally note that the fraction of mass contributed by high- and low-mass stars reported in Table 6 is an upper limit, because we did not account for mass loss from the zero-age main

Table 6. MF exponent, low-mass to visible stars number ratio, high-mass to visible stars number ratio, low-mass to visible stars mass ratio, high-mass to visible stars mass ratio and total invisible (low + high mass) to visible stars mass ratio.

s	N_l/N_v	N_h/N_v	M_l/M_v	M_h/M_v	M_i/M_v
−2.68	0.341	30.5	1.24	5.61	6.85
−2.72	0.305	36.6	1.07	6.74	7.81

sequence (ZAMS) to remnants and for stars escaping the cluster over its lifetime.

9.2 The contribution of the Milky Way gravitational field

Danilov & Loktin (2015) proposed a formula for dynamical evaluation of star cluster mass accounting for the Galactic gravitational field and for non-stationarity of the cluster:

$$M_d = \frac{2\bar{R}R_u\left[2\sigma^2 - \frac{(\alpha_1+\alpha_3)\langle r^2\rangle}{3}\right]}{G(\bar{R}+R_u)}, \quad (19)$$

where $R_u = \langle 1/r_i\rangle^{-1}$ is the mean inverse star distance to the cluster centre, $\bar{R} = \langle 1/r_{ij}\rangle^{-1}$ is the mean inverse star-to-star distance, $\langle r^2\rangle$ is the mean square of the star distance to the cluster centre and α_1 and α_3 are the field constants (Chandrasekhar 1942) characterizing the Galactic potential, $\Phi(R, z)$ in Galactocentric cylindrical coordinates, in the vicinity of a star cluster:

$$\alpha_1 = \left(\frac{1}{R}\frac{\partial\Phi}{\partial R} - \frac{\partial^2\Phi}{\partial^2 R}\right)_{R_{cl}} = 4A(B-A) < 0, \quad (20)$$

where A and B are Oort's constants and

$$\alpha_3 = -\left(\frac{\partial^2\Phi}{\partial^2 z}\right)_{z_{cl}} > 0. \quad (21)$$

R_{cl} and z_{cl} are the cluster centre-of-mass cylindrical coordinates. The values of α_1 and α_3 were calculated adopting the Galactic potential model of Kutuzov & Osipkov (1980). Arguments in favour of this model are listed in Seleznev (2016).

The error in the radial velocity dispersion was estimated by the formula $D\sigma^2 \approx 2\sigma^4/N$ from Cramer (1946).

To estimate values of $\bar{R}$, R_u and $\langle r^2\rangle$, we obtain the spatial distribution of stars around the cluster centre by Monte Carlo sampling of the spatial density profile $f(r)$ as obtained by deprojecting the observed surface density profile $F(r)$ of the cluster (von Zeipel & Lindgren 1921). Our technique requires a numerical differentiation of $F(r)$, which is not a problem because we adopt a kernel estimate of $F(r)$, which is a differentiable function:

$$f(r) = \frac{1}{\pi}\int_0^{\sqrt{R_c^2-r^2}} S(\sqrt{r^2+x^2})\,dz, \quad (22)$$

where

$$S(r) = -\frac{1}{r}\frac{dF(r)}{dr}. \quad (23)$$

20 different Monte Carlo samples were built, in order to estimate the scatter in the estimates. For the spatial density profile corresponding to $V_{lim} = 20$ mag, the following estimates were obtained: $\bar{R} = 2.71 \pm 0.14$ pc, $R_u = 1.84 \pm 0.16$ pc and $\langle r^2\rangle = 7.20 \pm 0.71$ pc^2 (the spatial density profile for $V_{lim} = 20$ mag was chosen, because for this limiting magnitude the surface density profile is steadily decreasing, which is of critical importance for deprojecting).

With these values of the mean stellar distribution characteristics, the following estimates of the cluster masses were obtained: $M_{vir} = 10\,100 \pm 2200\,M_\odot$ and $M_d = 8200 \pm 2500\,M_\odot$, where

$$M_{vir} = \frac{2\sigma^2\bar{R}}{G}. \quad (24)$$

There are two possible explanation for the large difference between the dynamical and virial mass estimates on the one hand and the star-count mass estimates on the other hand. One possibility is that star counts did not reveal the vast cluster corona (due to a relatively small field or large fluctuation of the field stellar density in the case of star counts with the 2MASS catalogue), so that the mass estimates obtained by star counts and the mass function are underestimated. Recall that mass estimates obtained with density profiles or the mass function are lower ones, because of the unknown low-mass end of the stellar mass distribution and unaccounted-for unresolved binaries and probable remnants of massive stars.

Another possibility is that the velocity dispersion, upon which dynamical estimates are based, is overestimated. One reason for that could be binarity, because binary revolution orbital motion tends to enlarge velocity dispersion.

We can use equation (14) to estimate what value of velocity dispersion corresponds to the cluster mass estimates obtained with the surface density profiles and with the mass function. The mass estimate $1880 \pm 820\,M_\odot$ corresponds to a total dispersion of 1.39 ± 0.38 km s^{-1} and a radial velocity dispersion of 0.80 ± 0.22 km s^{-1}, assuming $\sigma_r = \sigma/\sqrt{3}$. The mass estimate $1820 \pm 620\,M_\odot$ corresponds to a total dispersion of 1.37 ± 0.29 km s^{-1} and a radial velocity dispersion of 0.79 ± 0.17 km s^{-1}.

10 SUMMARY AND CONCLUSIONS

In this work, we exploited photometric and spectroscopic material to derive the present-day mass of the Galactic star cluster NGC 4337. The star-count mass was derived both from the cluster density profile ($1820 \pm 620\,M_\odot$) and from the cluster luminosity function ($1880 \pm 820\,M_\odot$). The two estimates generally overlap. The dynamical mass, estimated in the assumption of virial equilibrium, is significantly larger ($M_3 = 11\,400 \pm 4550\,M_\odot$). Considering the Galactic gravitational field and non-stationarity of the cluster results in a smaller estimate of $M_d = 8200 \pm 2500\,M_\odot$. In any case, this smaller estimate exceeds the star-count mass by at least 4.4 times. The possible contribution of invisible low-mass stars and high-mass star remnants increases the cluster mass considerably (7.85 or 8.81 times, depending on the adopted slope of the cluster mass function; see Table 6). The luminous and dynamical mass could become comparable if one takes into account this contribution and mass loss from the ZAMS to remnants and stars escaping the cluster over its lifetime. Another possible source of the discrepancy between star-count and dynamical mass estimates could be an undetected vast cluster corona (due to a relatively small field or large fluctuation of the field stellar density) or overestimated velocity dispersion value (due to inclusion of unresolved binary stars in the sample, for example).

It is interesting at this point to try to reconstruct whether NGC 4337 suffered from significant mass loss and infer an estimate of its initial mass. This would help us to understand the reasons why it appears less dynamically evolved than its twin NGC 752.

We estimated the initial mass of the cluster by using three different measurements of the current mass of NGC 4337. We make

use of an approximate method accounting for mass loss due to stellar evolution, the Galactic tidal field and encounters with giant molecular clouds and spiral arms. We follow Dalessandro et al. (2015), who carried out the same exercise for the old metal-rich cluster NGC 6791, and we refer the reader to their work for a detailed description of the procedure, which is based on the theoretical study by Lamers et al. (2005). To derive an estimate of the cluster initial mass, several constants characterizing the cluster and the environment need to be adopted. To evaluate equation (1) of Dalessandro et al. (2015), we use $t = 1.6 \pm 0.1$ Gyr for the age of the cluster and the three mass estimates derived above: $m_1 = 1820 \pm 620\,M_\odot$ (Section 6), $m_2 = 1880 \pm 820\,M_\odot$ (Section 8) and $m_3 = 11\,400 \pm 4550\,M_\odot$ (Section 9).

To characterize the mass loss due to stellar evolution (equation 2 in Dalessandro et al. 2015), we use the metallicity $Z = 0.02$ (the coefficient given in Table 1 of Lamers et al. 2005), which is sufficiently close to the value of 0.025 estimated here. The tidal mass loss is characterized by the dissolution time-scale $t_0 = 3.3^{+1.4}_{-1.0}$ Myr. This value was derived for the solar neighbourhood and is a good approximation for the cluster NGC 4337, which is currently located at a Galactocentric radius of $\sim$7.8 $\pm$ 0.1 kpc. Finally, for the coefficient γ characterizing the initial density distribution, we adopt $\gamma = 0.62$, which is a typical value for open clusters (Baumgardt & Makino 2003).

We consider the uncertainty intervals for the current cluster age t, mass estimates $m_{1,2,3}$ and dissolution time-scale t_0, which has the largest influence on the initial mass estimate (Dalessandro et al. 2015). This leads to initial masses of about $m_{\rm ini,1} \approx 20$–$24 \times 10^3\,M_\odot$, $m_{\rm ini,2} \approx 19$–$24 \times 10^3\,M_\odot$ and $m_{\rm ini,3} \approx 35$–$53 \times 10^3\,M_\odot$. We note that these values represent a rough estimate and are based on an approximate method and parameters derived for average open clusters observed in the solar neighbourhood.

In the most reliable case of an actual mass estimate that includes remnants and low-mass stars, the cluster would have lost between 60 and 80 per cent of its initial mass.

ACKNOWLEDGEMENTS

The work of A. F. Seleznev and the science leave of G. Carraro in Ekaterinburg was supported by Act 211 Government of the Russian Federation, contract No. 02.A03.21.0006 and by the ESO DGDF programme. G. Baume acknowledges support from CONICET (PIP 112-201101-00301) and financial support from the ESO visitor programme that allowed a visit to ESO premises in Chile, where part of this work was done. This publication also made use of data from the Two-Micron All-Sky Survey, which is a joint project of the University of Massachusetts and the Infrared Processing and Analysis Center/California Institute of Technology, funded by the National Aeronautics and Space Administration and the National Science Foundation. We thank the Centre de Données Astronomiques de Strasbourg (CDS), the US Naval Observatory and NASA for the use of their electronic facilities, especially SIMBAD, ViZier and ADS, and the WEBDA data base.

This work was based on observations obtained at the Cerro Tololo Inter-American Observatory, Chile, and at ESO Paranal Observatory under programme 292.D-5043.

REFERENCES

Baume G., Carraro G., Momany Y., 2009, MNRAS, 398, 22
Baume G., Carraro G., Comeron F., de Elía G. C., 2011, A&A, 531, A73
Baumgardt H., Makino J., 2003, MNRAS, 340, 227
Bressan A., Marigo P., Girardi L., Salasnich B., Dal Cero C., Rubele S., Nanni A., 2012, MNRAS, 427, 127
Carraro G., Seleznev A., 2012, MNRAS, 419, 3608
Carraro G., Baume G., Piotto G., Mendez R. A., Schmidtobreick L., 2005, A&A, 436, 527
Carraro G., Giorgi E., Costa E., Vazquez R. A., 2014a, MNRAS, 441, L36
Carraro G., Monaco L., Villanova S., 2014b, A&A, 568, A86
Chandrasekhar S., 1942, Principles of Stellar Dynamics. Univ. Chicago Press, Chicago, IL
Chumak Y. O., Platais I., McLaughlin D. E., Rastotguev A. S., Chumak O. V., 2010, MNRAS, 402, 1841
Coelho P., Barbuy B., Meléndez J., Schiavon R. P., Castilho B. V., 2005, A&A, 443, 735
Cramer H., 1946, Mathematical Methods of Statistics. Princeton Univ. Press, Princeton, NJ
Cutri R. M. et al., 2003, VizieR Online Data Catalog: II/246. CDS, Strasbourg, France
Dalessandro E., Miocchi P., Carraro G., Jilkova L., Moitinho A., 2015, MNRAS, 449, 1811
Danilov V. M., Loktin A. V., 2015, Astrophys. Bull., 70, 414
Danilov V. M., Seleznev A. F., 1994, Astron. Astrophys. Trans., 6, 85
Danilov V. M., Matkin N. V., Pylskaya O. P., 1985, SvA, 29, 621
Davenport J. R. A., Sandquist E. L., 2010, ApJ, 711, 559
Davies B., Bastian N., Gieles M., Seth A. C., Mengel S., Konstantopoulos I. S., 2011, MNRAS, 411, 1386
Geller A. M., Latham D. W., Mathieu R. D., 2015, AJ, 150, 97
Kharchenko N. V., Berczik P., Petrov M. I., Piskunov A. E., Röser S., Schilbach E., Scholz R.-D., 2009, A&A, 495, 807
Kutuzov S. A., Osipkov L. P., 1980, SvA, 24, 17
Lamers H. J. G. L. M., Gieles M., Bastian N., Baumgardt H., Kharchenko N. V., Portegies Zwart S., 2005, A&A, 441, 117
Landolt A. U., 1992, AJ, 104, 372
Lupton R., 1993, Statistics in Theory and Practice. Princeton Univ. Press, Princeton, NJ
Merritt D., Tremblay B., 1994, AJ, 108, 514
Pancino E., Seleznev A., Ferraro F. R., Bellazzini M., Piotto G., 2003, MNRAS, 345, 683
Prisinzano L., Carraro G., Piotto G., Seleznev A., Stetson P. B., Saviane I., 2001, A&A, 369, 851
Seleznev A. F., 2016, MNRAS, 456, 3757
Seleznev A. F., Carraro G., Costa E., Loktin A. V., 2010, New Astron., 15, 61
Silverman B. W., 1986, Monographs on Statistics and Applied Probability. Chapman and Hall, London
Skrutskie M. F. et al., 2006, AJ, 131, 1163
Stetson P. B., 1987, PASP, 99, 191
Tofflemire B. M., Gosnell N. M., Mathieu R. D., Platais I., 2014, AJ, 148, 61
Twarog B. A., Anthony-Twarog B. J., Deliyannis C. P., Thomas D. T., 2015, AJ, 150, 134
von Zeipel H., Lindgren J., 1921, Kgl. Svenska Vet. Akad. Handlingar, 61, 15

This paper has been typeset from a TEX/LATEX file prepared by the author.